



Noble-metal-free MnS/In₂S₃ composite as highly efficient visible light driven photocatalyst for H₂ production from H₂S

Meng Dan ^{a,b}, Qian Zhang ^b, Shan Yu ^b, Arvind Prakash ^b, Yuanhua Lin ^{a,b}, Ying Zhou ^{a,b,*}

^a State Key Laboratory of Oil and Gas Reservoir Geology and Exploitation, Southwest Petroleum University, Chengdu 610500, China

^b The Center of New Energy Materials and Technology, School of Materials Science and Engineering, Southwest Petroleum University, Chengdu 610500, China

ARTICLE INFO

Article history:

Received 2 March 2017

Received in revised form 26 April 2017

Accepted 7 June 2017

Available online 9 June 2017

Keywords:

Photocatalysis

Hydrogen

H₂S

MnS/In₂S₃ composite

Quantum efficiency

ABSTRACT

Large amounts of sulfide or sulfite have been extracted from fossil energy resources, which call for green strategies to utilize them. In this study, hydrogen production and H₂S removal are simultaneously achieved over MnS/In₂S₃ composite photocatalysts. Highly active MnS/In₂S₃ composite photocatalysts were synthesized via a solvothermal route. The photocatalytic activities depend on their compositions. A maximum H₂ production rate of 8360 μmol g⁻¹ h⁻¹ can be achieved over a MnS/In₂S₃ with optimized composition, which is approximately 2090 times higher than that of pristine α-MnS and 50 times higher than that of β-In₂S₃ alone. The corresponding quantum efficiency of this sample is as high as 34.2% at 450 nm even in the absence of any noble-metal co-catalysts. Importantly, MnS/In₂S₃ composite displays a good stability and anti-photocorrosion, which provides a strategy for scaling up the H₂ production from byproducts at petrochemical plants for energy applications.

© 2017 Elsevier B.V. All rights reserved.

1. Introduction

With the use and depletion of fossil fuels, environmental pollution and energy shortage are becoming the most urgent global issues that we face today [1]. Currently, ca. 80% of the total world energy supply is still covered by fossil fuel combustion despite the emergence of new energy resources [2]. Consumption of fossil fuels can produce high levels of harmful gases and waste residues. Most seriously, it can cause a range of environmental problems such as global warming, climate change and melting of polar ice, etc. Instead, hydrogen is a logical option as energy carrier for future society, given its high energy capacity and environmentally friendly properties. However, at present hydrogen is mainly produced from fossil fuels such as natural gas by steam reforming, which goes along with large amounts of CO₂ emission and energy consumption. Fortunately, Fujishima and Honda laid the foundation for hydrogen evaluation from the decomposition of water on a TiO₂ electrode under UV light irradiation already in 1972 [3], opening up new avenues for the green production of hydrogen.

Over the past years, researchers have extensively studied the photocatalytic production of hydrogen through splitting of water [4,5]. Apart from water, hydrogen sulfide (H₂S) is also a potential source of hydrogen, because the cleavage of H₂S is much easier than H₂O. The required ΔG for splitting H₂S is only 39.4 kJ mol⁻¹, which is much less than 284.7 kJ mol⁻¹ required for water splitting [6,7]. Additionally, H₂S is very harmful to animals and human beings. For example, the concentration of H₂S higher than 320 ppm in air result in pulmonary edema, and concentrations above 700 ppm are deadly [8]. Currently, the Claus process is being widely used for the decomposition of H₂S via the following reaction: H₂S + 1/2O₂ → H₂O + S [9]. However, this process is energy consuming and leads to serious environmental issues due to the generation of hazardous by-products, e.g. SO_x. Especially, the hydrogen energy stored in H₂S is not reclaimed in the Claus process [10–12]. Therefore, green and facile routes are now demanded to convert hazardous and corrosive gaseous (H₂S) into clean energy (H₂). Recently, photocatalytic splitting of H₂S has attracted great attention. Nevertheless, the development of highly active visible-light-driven photocatalysts for H₂ production from of H₂S is still a tremendous challenge.

Numerous metal oxides, such as SrTiO₃ [13,14], ZnO [15], Bi₂O₃, [16], and TiO₂ [17,18] have been reported for photocatalytic water splitting due to their suitable band structures in combination with

* Corresponding author at: State Key Laboratory of Oil and Gas Reservoir Geology and Exploitation, Southwest Petroleum University, Chengdu 610500, China.

E-mail address: yzhou@swpu.edu.cn (Y. Zhou).

non-toxic and stable properties. In principle, these oxide materials can be directly used for photocatalytic splitting of H₂S as well [19–23]. However, various challenges need to be addressed for metal oxides when used as photocatalyst for splitting H₂S [24–28]. For instance, catalyst deactivation was commonly observed in H₂S splitting because metal sulphide has far lower solubility than metal oxide [24,25]. In addition, to achieve high quantum yields and photocatalytic activity, noble-metals were widely used as co-catalysts. Unfortunately, they are very expensive and are easily deactivated in the presence of small amounts of H₂S species [26]. On the other hand, some metal sulphides including CdS [29–31], Bi₂S₃ [32], and CdIn₂S₄ [33] have been proposed for visible-light photocatalytic H₂ production from H₂S. The valence band (VB) of metal sulfides consists of S 3p orbitals, which are higher than the O 2p orbital, resulting in relatively narrow band gaps [4]. Therefore, metal sulfides generally exhibit strong visible-light absorption for efficient utilization of solar energy [34]. More importantly, the sulfur content of metal sulphides may help to reduce catalyst deactivation through H₂S. Unfortunately, metal sulfides frequently suffer from photocorrosion during the photocatalytic reaction [35]. Moreover, the photo-generated S_n²⁻ can be adsorbed on the catalyst surface which could not only occupy the active sites but also shield the light absorption [36]. Hence, the long-term photocatalytic H₂ production from H₂S was rarely reported and typically only the activity in the first 3–5 h was indicated (cf. Table S1). This calls for the development of efficient non-noble-metal photocatalysts with visible-light response and long-term stability.

Manganese sulfide (MnS), an important magnetic semiconductor with a wide band gap ($E_g(T=0) \approx 3.7$ eV), has drawn remarkable interest because of its unique attributes and potential applications in optoelectric devices, luminescence, solar cell and especially photocatalysis [37,38]. However, its wide band gap limits the light response range. In recent years, much attention has been focused on finding a way to overcome these disadvantages. Constructing the composite heterostructures seems to be an efficient way for this matter [39]. For example, MnS/CdS [40,41], MnS/Cu₇S₄ [42], MnS/Cu₂S [43] MnS/FeS [44] have been designed and established for realizing the wide applications of MnS in photocatalysis area. Herein, CdS, Cu₇S₄, Cu₂S and FeS present a similar characteristic: the relatively narrow band gap energy. However, In₂S₃ is a n-type semiconductor with a narrow band gap of 2.0–2.3 eV, and is a potential candidate for photocatalytic application because of its suitable band gap for solar energy conversions [45,46]. But, it exhibits relatively low photocatalytic activity when used as a single catalytic for photocatalytic reaction due to its low charge separation ability. Therefore, the formation of MnS/In₂S₃ heterostructure composite can efficiently promote charge separation and optical absorption. Similarly, it could induce a synergistic effect between MnS and In₂S₃. To the best of our knowledge, MnS/In₂S₃ heterostructure composite is barely studied for photocatalysis before.

Herein, a series of nanostructured MnS/In₂S₃ heterostructure composites were successfully prepared by a one-pot solvothermal method. The crystal structure and morphology of the obtained MnS/In₂S₃ composites are strongly affected by the molar ratios of the Mn(CH₃COO)₂·4H₂O and InCl₃ precursors. The formed 2D layered heterostructures between γ -MnS and β -In₂S₃ can lead to large contact area and intimate contact, thus exhibiting highly enhanced visible light photocatalytic activity. To the best of our knowledge, this is the first time that MnS/In₂S₃ composites are reported to be very active in the visible-light photocatalytic H₂ production from H₂S with a maximum activity of 8360 $\mu\text{mol h}^{-1} \text{ g}^{-1}$. Their apparent quantum yield (QE) is as high as 34.2% at 450 nm even in the absence of noble-metal co-catalyst, corresponding to H₂ evolution amount of 36440 $\mu\text{mol h}^{-1}$. Importantly, their resistance against photocorrosion and long-term stability can be significantly improved through the addition of S²⁻ and SO₃²⁻ ions. Finally, the

photocatalytic H₂ production process over MnS/In₂S₃ composite is discussed.

2. Experimental

2.1. MnS/In₂S₃ composites prepared by solvothermal method

The composite sulfide system, MnS/In₂S₃, was synthesized by a one-pot solvothermal method. In a typical synthesis procedure, Mn(CH₃COO)₂·4H₂O (2 x mmol), InCl₃ (2–2 x mmol) and thioacetamide (TAA) (9.0 mmol) were dissolved into 25 mL pyridine to form a homogeneous solution. For convenience, the MnS/In₂S₃ composites were denoted as MnS/In₂S₃·0.1, MnS/In₂S₃·0.3, MnS/In₂S₃·0.5, MnS/In₂S₃·0.6, MnS/In₂S₃·0.7, MnS/In₂S₃·0.8 and MnS/In₂S₃·0.9, corresponding to the x value of 0.1, 0.3, 0.5, 0.6, 0.7, 0.8, and 0.9, respectively. The obtained solution was immediately transferred into a Teflon-lined stainless steel autoclave with 50 mL inner volume. Then, the autoclave was maintained at 180 °C for 18 h. After cooling to room temperature naturally, the prepared precipitates were centrifuged and washed several times with ethanol and acetone. Finally, the obtained powders were dried at 55 °C for 10 h.

2.2. Characterization

The structure and crystallinity of the samples were investigated by X-ray diffraction (XRD) (PANalytical X'pert) with Cu K α radiation operated at 40 kV/40 mA. The elements in the composites were determined by inductively coupled plasma atomic emission spectrometry (ICP, Varian ES) after the samples were dissolved in a mixture solution of HNO₃ and HCl. Scanning electron microscopy (SEM) and energy dispersive X-ray spectroscopy (EDXS) were performed on a JEOL JSM-7800F microscopy equipped with EDAX detector. Transmission electron microscopy (TEM) observations were collected on a Tecnai G2 F30 electron microscopy with an accelerating voltage of 200 kV. X-ray photoelectron spectroscopy (XPS) measurements were performed using a Thermo ESCALAB250Xi X-ray photoelectron spectrometer and all of the binding energies were referenced to the C 1s level at 284.8 eV. UV-vis diffuse reflectance spectra (DRS) were recorded at room temperature on a Shimadzu UV-2600 spectrophotometer equipped with an integrating sphere using Ba₂SO₄ as the reflectance standard. The photoluminescence (PL) spectra were measured with a fluorescence spectrophotometer (Nicolet 6700). The N₂ sorption isotherm and Brunauer-Emmett-Teller (BET) surface area were determined by the nitrogen adsorption method (Quadasorb SI). The samples were degassed at 110 °C for 8 h under vacuum before measurements.

2.3. Photocatalytic performance evaluation

The photocatalytic activity measurements were conducted in a home-made photoreactor (50 mL Pyrex flask). Fig. S1 shows the schematic diagram of this setup, which contains three parts including H₂S generation (I), photodecomposition of H₂S (II) and tail-gas unit (III). Firstly, 2.5 mg of catalyst powders were suspended through ultrasonication for 25 min in an aqueous solution (50 mL) containing Na₂S (0.1 mol L⁻¹) and Na₂SO₃ (0.6 mol L⁻¹). Then, the reactor was purged with Ar for 30 min followed by bubbling 3 M H₂S in the solution for 3 h at room temperature. After the injection of 1 mL CH₄ gas used as internal standard, the reactor was illuminated by a 300-W Xe lamp with a cutoff filter ($\lambda > 420$ nm). The amount of produced hydrogen was monitored using a Shimadzu GC-2010 Plus gas chromatograph (GC) (Ar carrier gas, molecular sieve 5 Å, TCD detector).

The apparent quantum yield (QE) was calculated according to Eq. (1). The number of evolved H₂ molecules was measured by GC (Shimadzu GC-2010 Plus) and the number of incident photons at 450 nm was determined from the output of a monochromatic LED lamp (100 mW/cm²).

$$\text{QE}(\%) = \frac{\text{number of reacted electrons}}{\text{number of incident photons}} \times 100 \quad (1)$$

$$= \frac{2 \times \text{number of evolved H}_2 \text{ molecules}}{\text{number of incident photons}} \times 100$$

2.4. Photoelectrochemical measurements

Photocurrents were conducted by using CHI660E electrochemical work station (Chenhua Instrument, Shanghai, China) with a standard three-electrode system. The working electrode with an active area of ca. 4 cm² was prepared by a doctor blading technique (film thickness: ca. 50 μm), and subsequently treated at 180 °C for 2 h. The counter electrode was a Pt wire and saturated calomel electrode (SCE) as the reference electrode. A sacrificial reagents aqueous solution (0.1 M Na₂S and 0.6 M Na₂SO₃) was used as electrolyte. The photocurrent measurements over all the samples at open circuit potential were tested under visible-light irradiation ($\lambda > 420$ nm), and under chopped illumination with 100 s light on/off cycles.

3. Results and discussion

3.1. Structure, composition and morphology

Fig. 1 shows the XRD patterns of the prepared samples with different molar ratios of Mn(CH₃COO)₂·4H₂O and InCl₃ precursors. In the absence of InCl₃, the diffraction peaks are very sharp and intense indicating the good crystallinity, and all of the peaks can be indexed into cubic α-MnS (JCPDS 06-0518) (cf. Fig. 1a). With the addition of InCl₃, the formation of thermodynamically stable α-MnS was suppressed. The main Mn-based phase was hexagonal γ-MnS (JCPDS 40-1289) (Fig. 1b). These are in line with the previous reported Mn_{1-x}Cd_xS composites [47], where the formation of γ-MnS was accompanied by the disappearance of thermodynamically stable α-MnS [47]. With further increasing InCl₃ amounts, α-MnS disappeared completely. Instead, γ-MnS and β-In₂S₃ (JCPDS 65-0459) were observed (Fig. 1c–d). In the case of these samples, the diffraction peaks of β-In₂S₃ shifted to lower angle which is probably due to the expansion of the interplanar spacing. It is worth noting that the diffraction peaks of γ-MnS were also diminished with increasing indium and finally disappeared for MnS/In₂S₃.0.3 (Fig. 1e). During this process, the content of InCl₃ varied accordingly. Also, MnS experienced a transformation from α phase to γ phase, and was disappeared eventually. This phenomenon may be induced by the immense discrepancy of the solubility product constant [47,37]. The In₂S₃ has a solubility product of K_{sp} = 5.7 × 10⁻⁷³ as compared to that of MnS (K_{sp} = 4.65 × 10⁻¹⁴) due to rapid and frequent nucleation, followed by the selective growth of metastable MnS on the In₂S₃ nuclei. Since In₂S₃ have a relatively low solubil-

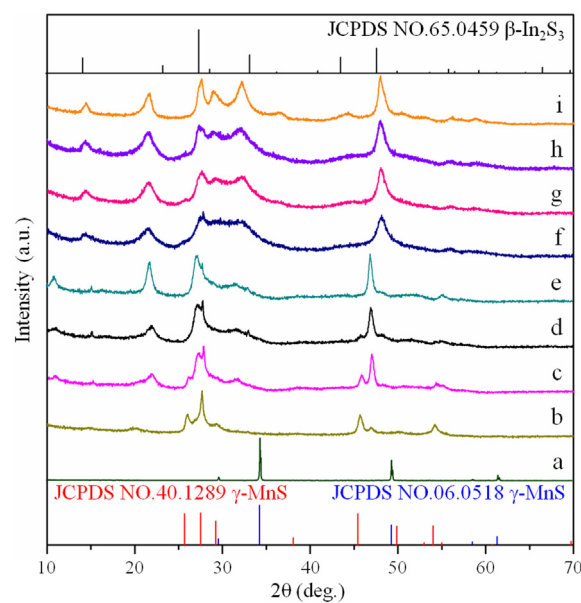


Fig. 1. XRD patterns of the prepared samples: (a) α-MnS; (b) MnS/In₂S₃.0.9; (c) MnS/In₂S₃.0.8; (d) MnS/In₂S₃.0.7; (e) MnS/In₂S₃.0.5; (f) MnS/In₂S₃.0.3; (g) β-In₂S₃.

ity product content, when the concentration of InCl₃ was equal or larger than that of Mn(CH₃COO)₂·4H₂O precursors, the growth of MnS was suppressed.

Considering the much difference of the solubility of In₂S₃ (K_{sp} = 5.7 × 10⁻⁷³) and MnS (K_{sp} = 4.65 × 10⁻¹⁴) [47–49], the real atomic ratios of In/Mn in the compositions were determined by ICP analysis. It was observed that the atomic ratios of In/Mn in the products were much different from the ratios of InCl₃/Mn(CH₃COO)₂·4H₂O precursors (Table S2). Especially, the In/Mn atomic ratios increased sharply when the original atomic ratio of In/Mn was equal or higher than 0.5 (Fig. S1 and Table S1). The N₂ adsorption/desorption isotherms of all MnS/In₂S₃ samples exhibit type IV with a typical H3 hysteresis loop (Fig. S3), which is characteristic of mesoporous materials [50]. The pore sizes and volumes of these samples determined by the Barrett-Joyner-Halenda (BJH) method are shown in Table S3. The BET surface area of MnS/In₂S₃ composites is between 12.0 and 37.3 m² g⁻¹ depending on the molar ratios of Mn and In precursors. These values are generally larger than those of pristine α-MnS (3.6 m² g⁻¹) and β-In₂S₃ (13.3 m² g⁻¹) (cf. Table 1). Hence, the formation of composites can enlarge the surface area and pore volume (Table S3) which is beneficial for photocatalytic efficiency. All in all, the molar ratios of Mn(CH₃COO)₂·4H₂O and InCl₃ precursors significantly influences the structure, composition and crystallinity of the products (Table 1).

The morphology of α-MnS, β-In₂S₃ and MnS/In₂S₃ composites was investigated by SEM (Fig. 2). In line with its cubic structure (Fig. 1), α-MnS displayed a cubic morphology in the range of several micrometers (Fig. 2a). After the addition of InCl₃ precursor, the cubic morphology was altered to a plant-like mor-

Table 1
Summary of properties of the MnS/In₂S₃ samples.

Samples	Composition	Specific surface area (m ² g ⁻¹)	Band gap (eV)	Rate of H ₂ evolution (μmol h ⁻¹ g ⁻¹)	QE (%)
α-MnS	Mn _{1.07} S	3.6	2.57	4	0.2
MnS/In ₂ S ₃ .0.9	Mn _{0.80} In _{0.13} S	12.0	2.80	1911	6.5
MnS/In ₂ S ₃ .0.8	Mn _{0.55} In _{0.30} S	37.3	2.51	2884	11.7
MnS/In ₂ S ₃ .0.7	Mn _{0.35} In _{0.43} S	32.9	2.48	8360	34.2
MnS/In ₂ S ₃ .0.5	Mn _{0.03} In _{0.65} S	24.6	2.38	1084	2.5
β-In ₂ S ₃	In _{1.97} S ₃	13.3	2.45	169	2.2

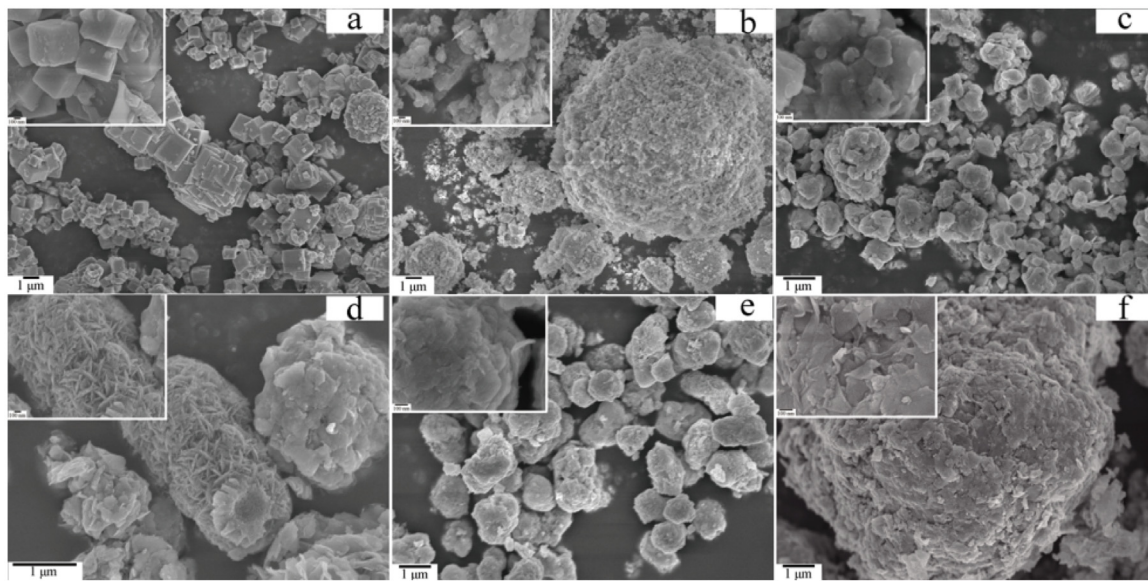


Fig. 2. SEM images of MnS/In₂S₃ samples: (a) α-MnS; (b) MnS/In₂S₃-0.9; (c) MnS/In₂S₃-0.8; (d) MnS/In₂S₃-0.7; (e) MnS/In₂S₃-0.5; (f) β-In₂S₃.

phology accompanying the phase change from α-MnS to γ-MnS (Figs. 1 and 2). With increasing amounts of InCl₃ precursor, a hierarchical morphology was observed (Fig. 2b–e). Among these products, MnS/In₂S₃-0.7 displays a well established flower-like morphology (Fig. 2d), whereas β-In₂S₃ shows a flake-like morphology (Fig. 2f). EDXS analysis confirmed the presence of S, Mn, In and O in all MnS/In₂S₃ samples (cf. Fig. S4). In addition, mapping of these three elements (S, Mn and In) showed that the distribution of these elements in the composites was uniform (Fig. S4).

As MnS/In₂S₃-0.7 exhibits interesting hierarchical morphology which could favor the photocatalytic reaction, this sample was selected for further investigation. The TEM and high resolution TEM (HRTEM) images of this sample were shown in Fig. 3. The presence of thin nanosheets was clearly observed (Fig. 3a), indicating that the building block of such hierarchical structures is 2D nanosheets. As can be seen from HRTEM image (Fig. 3b), the lattice spacing of 0.30 and 0.32 nm with a contact angle of 61.4° matches well with the (101) and (002) crystal planes of γ-MnS, whereas the lattice spacing of 0.26 nm and 0.19 nm with a contact of 45° matches well with the (400) and (440) crystal planes of β-In₂S₃. Importantly, the γ-MnS nanosheets are in close contact with the β-In₂S₃ to form 2D layered heterostructures, which is believed to promote the transfer of photogenerated electrons and holes between γ-MnS and β-In₂S₃, and suppresses their recombination [51–54]. Moreover, the (002)

crystal plane spacing of γ-MnS and (440) plane of β-In₂S₃ can be clearly observed in the selected area electron diffraction (SAED) pattern (inset of Fig. 3b). All of these results confirmed that the MnS/In₂S₃-0.7 sample consists of γ-MnS and β-In₂S₃ in accord with the XRD results (Fig. 1).

The surface chemical composition and binding environment of α-MnS, β-In₂S₃ and MnS/In₂S₃-0.7 were further investigated by XPS. An XPS survey of MnS/In₂S₃-0.7 indicates the presence of Mn, In, C, O and S in the composite (Fig. S5), which agrees well with the EDXS results (Fig. S4). The presence of C peak can be assigned to adventitious carbon species from XPS measurements. The two characteristic peaks at 653.6 and 642.0 eV in the spectra of α-MnS (Fig. 4a) are ascribed to Mn 2p_{1/2} and Mn 2p_{3/2}, which was separated by 11.6 eV in accord with the previous work [55]. Compared to α-MnS, these peaks in MnS/In₂S₃-0.7 shifted to 653.4 and 642.0 eV, respectively. The binding energy of In 3d_{3/2} and In 3d_{5/2} for β-In₂S₃ is identified at 452.7 and 445.1 eV (Fig. 4b), which can be assigned to In³⁺ in β-In₂S₃ [56]. After the formation of MnS/In₂S₃ composite, these peaks are shifted down by 0.3 eV. All of these results indicated the presence of strong interactions between MnS and In₂S₃ [57,58], which alternates the distribution of the electric charge of Mn and In. Fig. 4c shows the O 1s XPS spectra of α-MnS, β-In₂S₃ and MnS/In₂S₃-0.7, respectively. It is worth noting that the surface of all the samples contains O element, which could be ascribed to the sur-

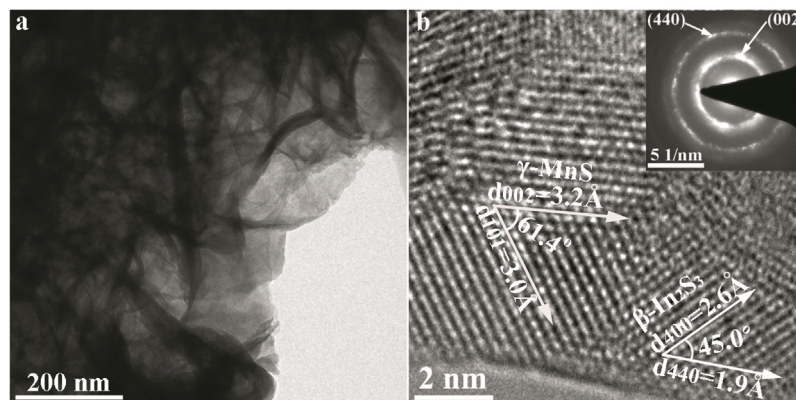


Fig. 3. (a) TEM and (b) HRTEM images of the MnS/In₂S₃-0.7 sample (inset is the corresponding SAED pattern).

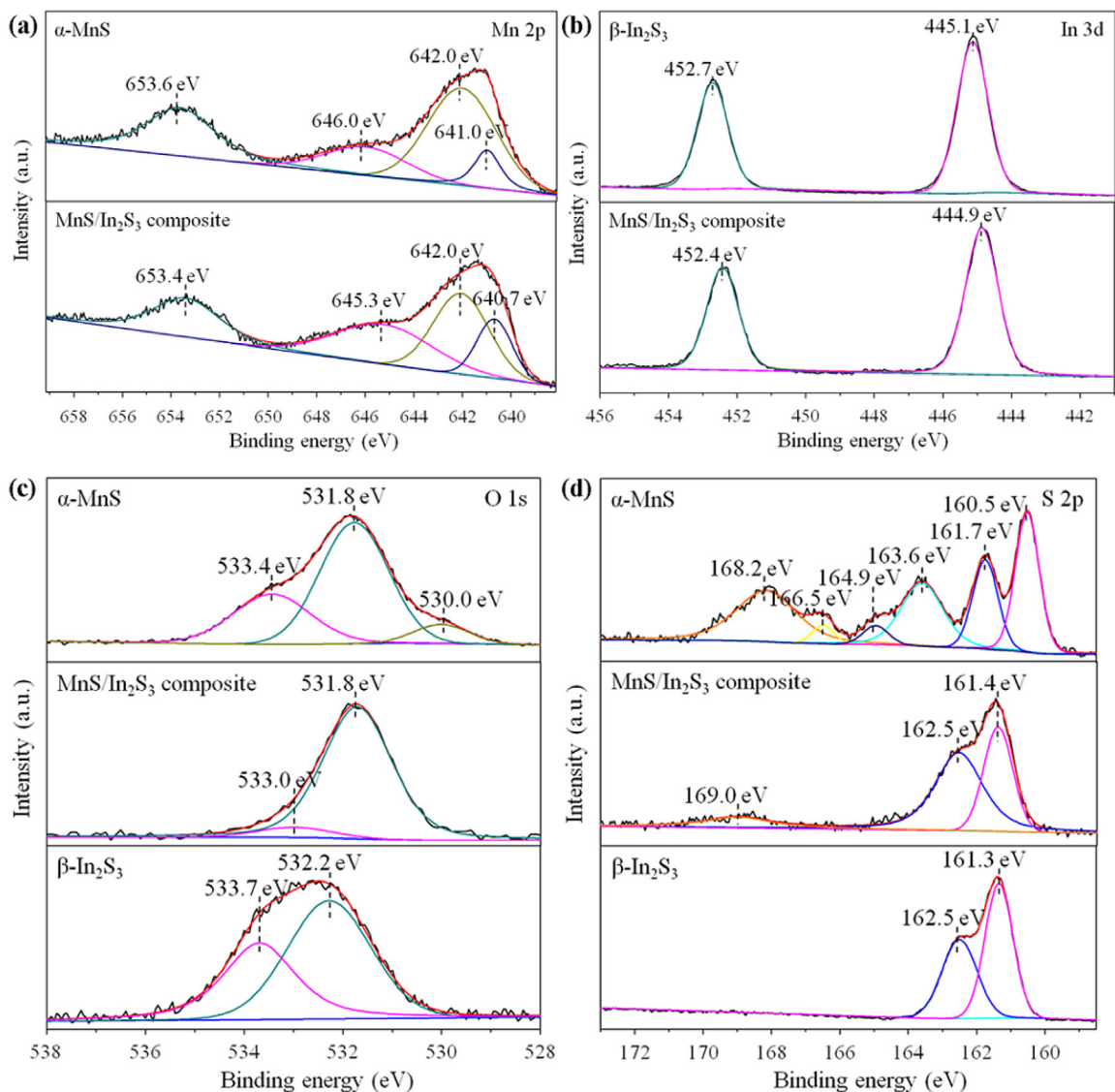


Fig. 4. (a) Mn 2p, (b) In 3d, (c) O 1s, and (d) S2p XPS spectra of α -MnS, β -In₂S₃ and MnS/In₂S₃.0.7 sample.

face adsorbed hydroxyl oxygen and water. Besides, as observed in Fig. 4d, the binding energies of S2p in MnS/In₂S₃.0.7 are 161.4 and 162.5 eV, which are higher than that of α -MnS (160.5 and 161.7 eV), and β -In₂S₃ (161.3 and 162.5 eV), which further confirmed the strong interaction between MnS and In₂S₃. Apart from the two main peaks mentioned above, several additional peaks were observed for α -MnS. The peaks located at 166.5, 164.9 and 163.6 eV can be assigned to thioacetamide or metal complex [59,60], whereas the peak at 168.2 eV corresponds to the sulphate species [61].

3.2. Optical properties

The UV-vis DRS of these prepared samples are shown in Fig. 5. The band gaps (E_g) can be calculated from the onset of the absorption edge and are summarized in Table 1. The E_g of α -MnS and β -In₂S₃ is 2.57 and 2.45 eV, respectively. Moreover, the E_g of MnS/In₂S₃ composites are strongly related to the molar ratio of Mn/In (Table 1). Notably, two additional absorption peaks in the visible light range (between 450 and 550 nm) were observed for α -MnS, which could be attributed to the internal transitions in the partly occupied 3d states of Mn and the bulk defects in crystals [62,63]. The absorption peak at 610 nm may be attributed to the

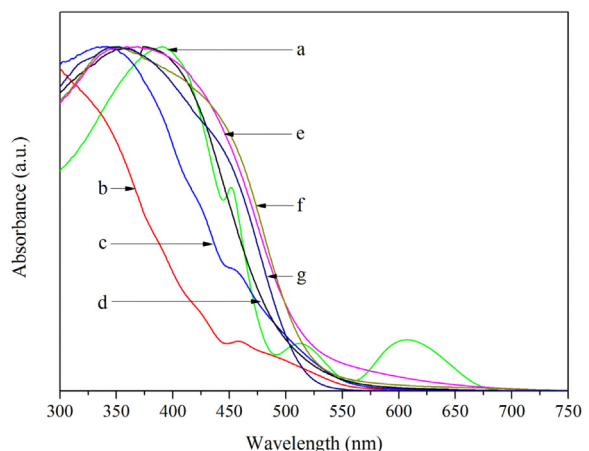


Fig. 5. UV-vis DRS of the obtained samples: (a) α -MnS; (b) MnS/In₂S₃.0.9; (c) MnS/In₂S₃.0.8; (d) MnS/In₂S₃.0.7; (e) MnS/In₂S₃.0.5; (f) MnS/In₂S₃.0.3; (g) β -In₂S₃.

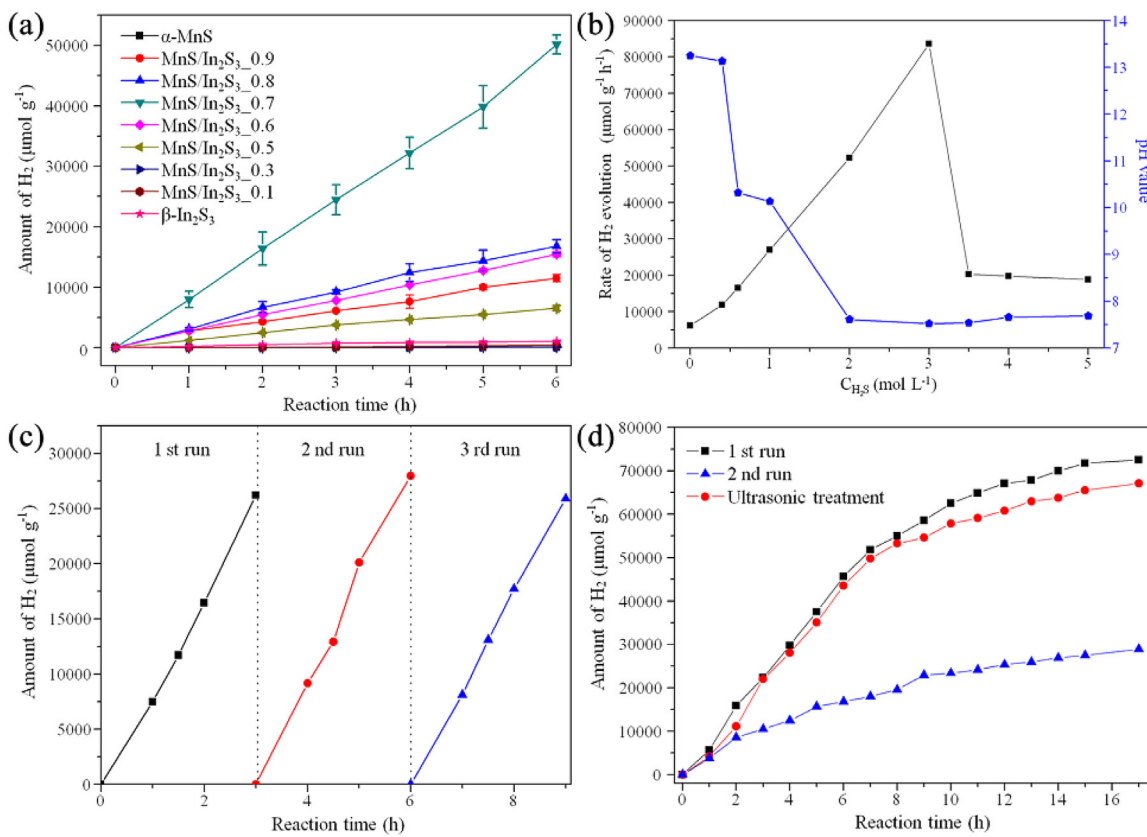


Fig. 6. (a) Photocatalytic H₂ production of these samples under visible light irradiation; (b) Dependence of H₂ production rate and pH value with the concentration of H₂S over MnS/In₂S₃_0.7; (c) Cycling experiments, (d) Long-term cycling experiments. Reaction conditions: catalyst, 2.5 mg; light source, 300 W Xe lamp with a cutoff filter ($\lambda > 420$ nm).

present of the metal complex. At low In percentage (MnS/In₂S₃_0.9 and MnS/In₂S₃_0.8), the absorption bands with shoulders were observed in the visible light region, demonstrating that a discontinuous level is formed by the dopants in the forbidden band due to the formation of doped photocatalysts (γ -(MnIn)S) [34,64,65]. All the samples exhibit obvious absorbance in the visible light range, indicating they have the potential for visible-light photocatalysis.

3.3. Photocatalytic performance

On the basis of UV-vis DRS analysis, it is reasonable to expect that these samples could be used as visible-light driven photocatalysts. The photocatalytic H₂ evolution over all the samples was tested under visible-light irradiation ($\lambda > 420$ nm) in Na₂S/Na₂SO₃ solution with 3 M H₂S for 6 h (Fig. 6a). No hydrogen production can be observed in the absence of either light irradiation or photocatalyst. Bare α-MnS and β-In₂S₃ exhibit a relatively poor activity for H₂ evolution (4 and 169 $\mu\text{mol g}^{-1} \text{h}^{-1}$, respectively, cf. Table 1 and Fig. S6). Upon the formation of MnS/In₂S₃ composites, the rate of H₂ evaluation remarkably increases and the photocatalytic activities depend on their compositions. Especially, it reaches a maximum value of 8360 $\mu\text{mol g}^{-1} \text{h}^{-1}$ for MnS/In₂S₃_0.7, which is approximately 2090 times higher than that with bare α-MnS and 50 times higher than that over β-In₂S₃ alone. The corresponding QE of this sample is as high as 34.2% at 450 nm even in the absence of any noble-metal co-catalysts, corresponding H₂ evolution amount of 36440 $\mu\text{mol h}^{-1}$. Meanwhile, it was observed that a significant amount of bubbles were produced during the photocatalytic reaction process (Movie S1), confirming the high activity of this sample. Considering the BET surface area of these samples was comparable

(Table 1), the enhanced photocatalytic activities cannot be solely ascribed to the surface area.

To understand the key role of 2D layered heterostructures between γ -MnS and β-In₂S₃ (Fig. 3) on the photocatalytic activity, another type of MnS/In₂S₃ sample with the same composition as MnS/In₂S₃_0.7 (Mn_{0.35}In_{0.43}S) was prepared by a simple mechanical stirring method (the detail preparation procedure can be found in Supporting information). For convenience, this sample was denoted as MnS/In₂S₃_mixture. The XRD and UV-vis DRS of this sample confirmed that it is a mixture of γ -MnS and β-In₂S₃ (Fig. S7). Most importantly, the rate of H₂ evolution over MnS/In₂S₃_mixture was approximately 50 times lower than that of the MnS/In₂S₃_0.7 (164 and 8360 $\mu\text{mol g}^{-1} \text{h}^{-1}$, respectively, cf. Fig. S7 and Table S4). Additionally, the rate of H₂ evolution over γ -MnS was approximately 360 times lower than that of the MnS/In₂S₃_0.7 (23 and 8360 $\mu\text{mol g}^{-1} \text{h}^{-1}$, respectively, cf. Fig. S7 and Table S4). These results clearly demonstrated the high activity of MnS/In₂S₃_0.7 is not only due to the compositions and instead, the formed 2D layered heterostructures between γ -MnS and β-In₂S₃ could play a very important role. Therefore, this sample (MnS/In₂S₃_0.7) was selected for further investigations. Firstly, the influence of the concentration of H₂S was considered as it can significantly change the pH value of the reaction system. Generally, the pH value decreases with increasing the concentration of H₂S and keeps stable (pH value in the range of 7.5–8.0) once the concentration of H₂S is higher than 2 M (Fig. 6b). Meanwhile, the photocatalytic H₂ production rate increases linearly with increasing the H₂S concentration up to 3 M. With further increasing the concentration of H₂S, the H₂ production rate was suddenly dropped (Fig. 6b). These results revealed that the optimized concentration of H₂S in our system is 3 M and the photocatalytic H₂ production is not only determined by pH values.

Table 2

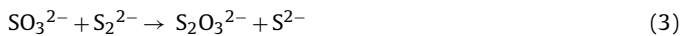
Photocatalytic H₂ production under visible light irradiation over MnS/In₂S₃.0.7 in different reaction medias.

Reaction medias	H ₂ production (μmol/g/h)	pH
3 M H ₂ S + 0.1 M Na ₂ S + 0.6 M Na ₂ SO ₃ (S1)	8360	7.55
3 M H ₂ S + 0.2 M NaOH + 0.6 M Na ₂ SO ₃ (S2)	4580	7.72
3 M H ₂ S + 0.2 M NaOH (S3)	130	7.65

Reaction conditions: volume of solution, 50 mL; catalyst, 0.0025 g MnS/In₂S₃.0.7; light source, 300 W Xe lamp with a cutoff filter ($\lambda > 420$ nm); reaction cell, Pyrex; pH = 7.5–8.0.

Considering the H₂ production experiments were performed in solution, H₂ could be from H₂O instead of H₂S. Therefore, various concentrations of KHC₈H₄O₄, HCl and H₂SO₄ were used to replace of H₂S and the pH was maintained in the range of 7.5–8.0 to exclude the influence of pH values. Particularly, no photocatalytic H₂ production was observed in the presence of KHC₈H₄O₄ or HCl, whereas the rate of H₂ evaluation is only 16 μmol g⁻¹ h⁻¹ in the presence of H₂SO₄ under the same reaction conditions, which is far less than that with H₂S (8360 μmol g⁻¹ h⁻¹) (Table S5). These results confirm the key role of H₂S in the production of H₂ in our current reaction condition.

Furthermore, in the current work, 0.6 M Na₂SO₃ and 0.1 M Na₂S were employed in reactant solutions. In general, Na₂SO₃ and Na₂S could play a role as the sacrificial reagents to consume photogenerated holes to improve the anti-photocorrosion ability of sulfide photocatalysts and promote H₂ evaluation [36]. To get insight into the role of Na₂SO₃ and Na₂S in the current reaction, we studied the photocatalytic H₂ evolution performance of MnS/In₂S₃.0.7 in different reaction medias including 0.1 M Na₂S/0.6 M Na₂SO₃ (S1), 0.2 M NaOH/0.6 M Na₂SO₃ (S2) and 0.2 M NaOH (S3) as NaOH is frequently used as absorbents for H₂S absorption and reaction media for H₂ production from H₂S [19,21,32,33]. Table 2 reveals the photocatalytic H₂ evolution rate over MnS/In₂S₃.0.7 in different reaction medias. The rate of H₂ evolution in the presence of S²⁻ and SO₃²⁻ (8360 μmol g⁻¹ h⁻¹) is significantly higher than that with SO₃²⁻ and OH⁻ (4580 μmol g⁻¹ h⁻¹) and with OH⁻ alone (130 μmol g⁻¹ h⁻¹). On the one hand, both SO₃²⁻ and S²⁻ can play a role as electron donors. On the other hand, the presence of S²⁻ ions in combination with the strong reducing action of SO₃²⁻ ions can prevent the formation of disulfide ions (S₂²⁻) [36,66]. The yellow S₂²⁻ can act as an optical filter to reduce the light absorption of catalysts [36], thus impacting their activity. According to Eqs. (2) and (3):



Colorless thiosulfate ions (S₂O₃²⁻), which does not reduce the light absorption of catalysts, could be formed instead of yellow S₂²⁻ under light irradiation. Therefore, the existence of S₂O₃²⁻ in solvent was investigated by the titration method [67]. The solution before and after photocatalytic reaction was mixed with an excess of starch solution (10 g L⁻¹). Then, S₂O₃²⁻ was back-titrated with I₂-KI solution (0.1 M). The results confirmed that no S₂O₃²⁻ was detected before photocatalytic reaction, while 175.13 μmol of S₂O₃²⁻ was observed after photocatalytic reaction for 6 h. All in all, these results indicated that S²⁻ and SO₃²⁻ are optimized reaction media which could not only enhance H₂ evaluation but also promote the formation of colorless S₂O₃²⁻ and favor long-term H₂ production.

Stability is another key factor to evaluate the performance of photocatalysts. MnS/In₂S₃.0.7 exhibits good anti-photocorrosion ability and photocatalytic stability under short-term illumination within three cycles (3 h each cycle) (Fig. 6c). Previously, most of the

work only reported the activity in the first 3–5 h for H₂ production from H₂S (Table S1) and the long-term stability of these catalysts was rarely known. Hence, we performed long-term recycling experiments. For the first run, the photocatalytic H₂ production rate over MnS/In₂S₃.0.7 increases linearly in the first 7 h. Then, the activity decreased slightly when the irradiation time exceeds 7 h (Fig. 6d). This phenomenon could be ascribed to the consumption of Na₂S/Na₂SO₃. Therefore, after the first run, the catalyst was collected by centrifugation and re-dispersed into the fresh aqueous solution containing 0.1 M Na₂S/0.6 M Na₂SO₃ solution with 3 M H₂S. Unfortunately, the activity of MnS/In₂S₃.0.7 is still much less than that in the first cycle, indicating that the deactivation cannot be mainly ascribed to the consumption of Na₂S/Na₂SO₃. Therefore, the MnS/In₂S₃.0.7 suspension was filtered and subsequently studied. Fig. S8 shows the XRD patterns of the sample before and after photocatalytic reaction. After the first run, orthorhombic sulfur (JCPDS 83-2284) was clearly observed in MnS/In₂S₃.0.7. These results indicated that sulfur could be simultaneously formed during the photocatalytic H₂ production process under long-term irradiation and then, deactivated the catalysts. Additionally, the XPS measurement was conducted to study chemical composition and binding environment of MnS/In₂S₃.0.7 after cycle. The result showed that the binding energy of Mn 2p, In 3d and O 1s for the MnS/In₂S₃.0.7 after cycle was not obviously changed. However, it is worth noting that the S 2p XPS spectra of MnS/In₂S₃.0.7 sample changed evidently as two additional peaks were observed. The peaks located at 168.4 and 163.5 eV can be assigned to silver thiosulfate [68,69] and sulfur [70] (cf. Fig. S9), respectively. This result also demonstrated that the formation of S and S₂O₃²⁻ in the reaction process. After ultrasonic treatment, sulfur can be easily removed from MnS/In₂S₃.0.7 (Fig. S8). Consequently, this catalyst is re-activated and exhibits comparable activity with the first run (Fig. 6d). This phenomenon illustrated that MnS/In₂S₃.0.7 had good stability in photocatalytic reaction process. Additionally, the atomic ratio of MnS/In₂S₃.0.7 sample after cycle was obtained by inductively coupled plasma (ICP) elemental analysis. The result revealed that the true composition of MnS/In₂S₃.0.7 sample after cycle was Mn_{0.35}In_{0.43}S, which was not changed as compared with MnS/In₂S₃.0.7 sample before photocatalytic reaction (cf. Table S2). All the evidences strongly confirmed that the MnS/In₂S₃.0.7 photocatalysts were extremely stable in the process of photocatalytic splitting H₂S into H₂.

3.4. Photocatalytic mechanism

It is well known that the separation and transfer of photo-generated electrons and holes for photocatalysis are the key steps which determine the photocatalytic efficiency. In order to investigate the photo-generated electrons and holes separation ability, the transient photocurrent response and photoluminescence spectrum of these samples were measured. As shown in Fig. 7a, all the samples show relatively stable and reversible photoreponses at light-on and light-off under visible-light irradiation. The MnS/In₂S₃.0.7 revealed the highest photocurrent of approximately 70 μA, indicating the efficient separation of photo-generated electrons and holes. In addition, it was observed that the photocurrent of MnS/In₂S₃.0.7 is also 22 times higher than that of MnS/In₂S₃.mixture (Fig. 7b), which agrees well with the photocatalytic activity evaluation (Fig. S7c). Fig. S10 shows the photoluminescence spectrum of these samples. It was observed that the emission intensity of MnS/In₂S₃.0.7 was significantly weakened, implying that the recombination of charge carriers was effectively decreased. Additionally, the emission peak was observed ca. 600 nm, which may be derived from the surface emissions and defects [71].

The efficient photocatalytic H₂ production usually requires sufficiently negative conduction band (CB) potential. The XPS valence

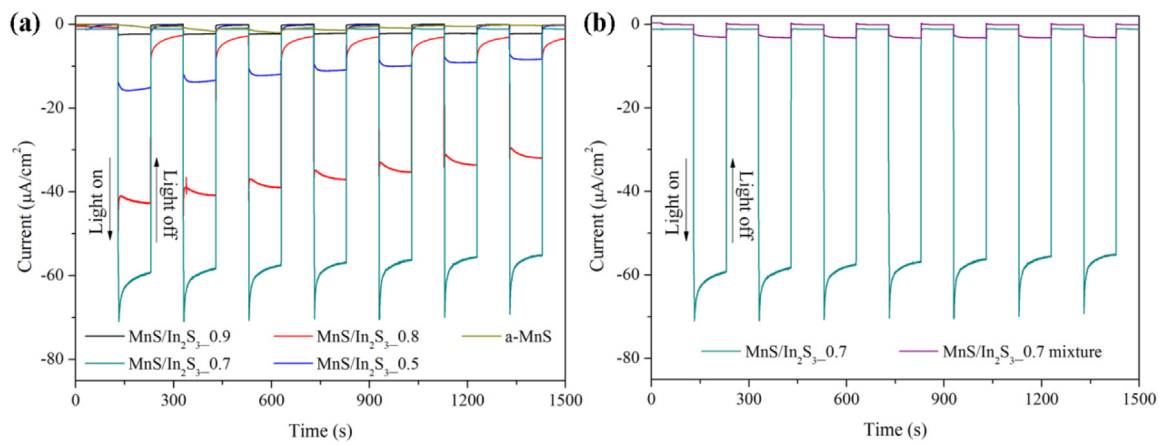


Fig. 7. Photocurrent response (I-t curve) of α -MnS (a); MnS/In₂S₃-0.9 (b); MnS/In₂S₃-0.8 (c); MnS/In₂S₃-0.7 (d); MnS/In₂S₃-0.5 (e) and MnS/In₂S₃-0.7 mixture (f) samples in the 0.1 M Na₂S and 0.6 M Na₂SO₃ electrolyte under visible light irradiation ($\lambda > 420$ nm).

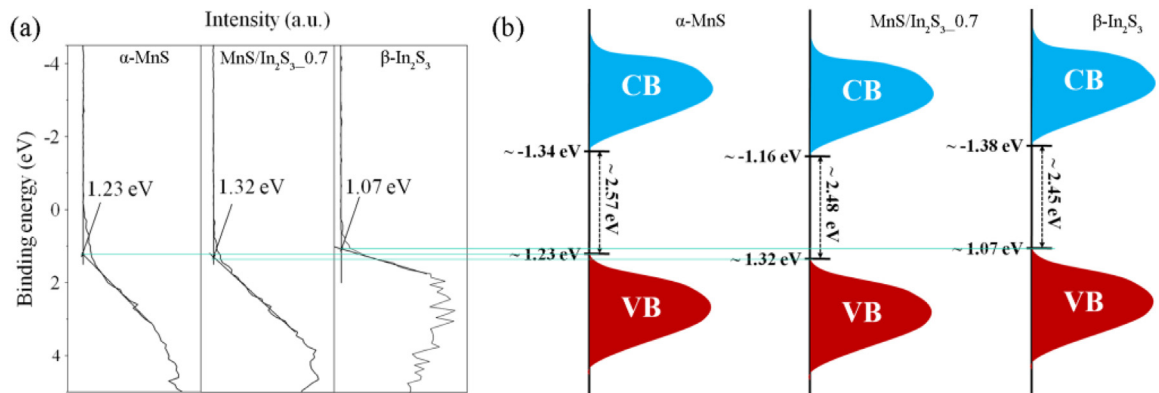
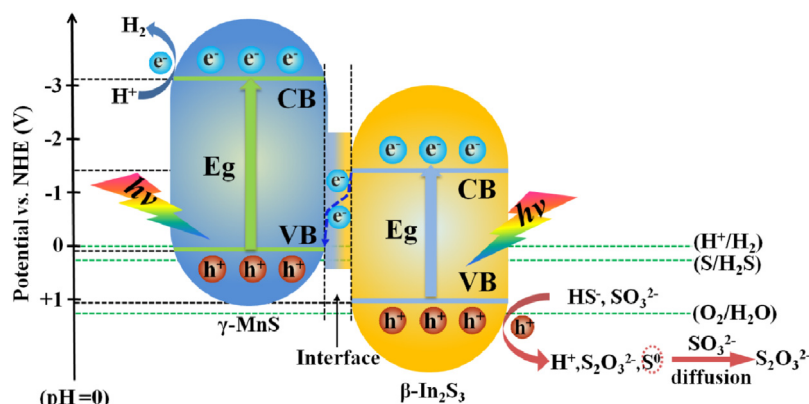


Fig. 8. (a) Valence-band XPS spectra and (b) band structure diagram of MnS/In₂S₃-0.7.

band (VB) spectra of MnS/In₂S₃-0.7 is shown in Fig. 8a. The VB maximum is located at 1.32 eV, whereas the E_g of this sample is 2.48 eV. Thus, the determined minimum of CB occurs at ~ -1.16 eV (Fig. 8b), which has a relatively appropriate redox potential for the photocatalytic H₂ production. Compared with the pure α -MnS and β -In₂S₃, the band structure of the MnS/In₂S₃-0.7 composite was changed accordingly.

Previously, the photocatalytic H₂ production from aqueous H₂S solution was normally performed in a strong base condition [19,21,32,33]. In our current reaction condition, the pH value is ca. 7.5–8.0 and the reaction process should be different from the

reaction under the strong base condition. The weak diprotic acid H₂S (two pK_a values are 7.0 and 11.96) dissociates and maintains equilibrium with HS⁻ ions. Additionally, to verify the band structure of γ -MnS, the valence-band XPS spectra of γ -MnS has been investigated (Fig. S11). The result shows that the valence band of γ -MnS is 0.05 eV. Therefore, its conduction band should be 3.15 eV according to the bandgap of 3.2 eV analyzed from UV-vis spectrum (Fig. S7). On the basis of the above results, the photocatalytic H₂ evaluation process is proposed as in Scheme 1. In such a reaction, the oxidation process is crucial. Accordingly, the oxidation process could be mainly divided into two steps: (1) photo-oxidation of HS⁻



Scheme 1. Photocatalytic process of splitting H₂S in 0.6 M Na₂SO₃/0.1 M Na₂S/3 M H₂S solution.

and $\text{SO}_3^{2-}/\text{S}^{2-}$ to S and $\text{S}_2\text{O}_3^{2-}$ ions by photogenerated holes over $\text{MnS}/\text{In}_2\text{S}_3$, (2) diffusion of S through the reaction with SO_3^{2-} from the surface of $\text{MnS}/\text{In}_2\text{S}_3$ to bulk solution. Preventing the formation of yellow S_2^{2-} and solid S leads to an impressively high H_2 production rate and improves the long-term stability.

The major reaction steps in this mechanism under visible light irradiation are described in following equations.



When γ -MnS and β - In_2S_3 samples were irradiated by a photon with sufficient energy equal or larger than E_g , both γ -MnS and β - In_2S_3 are excited, and the photogenerated electrons and holes are in their conduction and valence bands, respectively. Subsequently, the photogenerated electrons of β - In_2S_3 can transfer to γ -MnS due to the suitable energy band match between the CB of β - In_2S_3 and VB of γ -MnS, and recombine with the photogenerated holes of γ -MnS, leaving behind the electrons in the CB of γ -MnS and holes in the VB of β - In_2S_3 . The photogenerated valence holes (h^+) can oxidize HS^- and SO_3^{2-} ions to form S and $\text{S}_2\text{O}_3^{2-}$ ions, according to Eqs. (6) and (9), respectively. The CB electron (e^-_{CB}) can reduce protons liberated from the HS^- ions to produce molecular hydrogen. This process indicates hydrogen is produced from H_2S . According to Eq. (7), water may be also involved in the H_2 production. However, considering our reaction performed under pH 7.5–8.0, this effect should be insignificant due to the low concentration of proton in neutral water [72]. Moreover, almost no H_2 evaluation was observed in the absence of H_2S (cf. Table S5), further confirming this issue.

Compared to the previously reported H_2S splitting in strong base conditions, the combination of SO_3^{2-} and S^{2-} in the reaction exhibits three main advantages. Firstly, both SO_3^{2-} and S^{2-} in solution are electron donors, whereas OH^- has not this function and can only play a role as absorbent. Secondly, the addition of SO_3^{2-} and S^{2-} can prevent the formation of yellow S_2^{2-} and solid S. Finally, the solution with 0.6 M Na_2SO_3 /0.1 M Na_2S can maintain the pH value (7.5–8.0), which offer the maximum HS^- ions concentration ($\text{pK}_{\text{a}2}$ values are 7.0).

4. Conclusions

In summary, a series of $\text{MnS}/\text{In}_2\text{S}_3$ composites were successfully fabricated by a solvothermal method. It was found that $\text{MnS}/\text{In}_2\text{S}_3$ composites are very active for visible light photocatalytic H_2 production from H_2S . The photocatalytic activities are strongly related to their compositions. A maximum H_2 production rate of $8360 \mu\text{mol g}^{-1} \text{h}^{-1}$ can be achieved over $\text{MnS}/\text{In}_2\text{S}_3_0.7$ ($\text{Mn}_{0.35}\text{In}_{0.43}\text{S}$) catalyst, which is approximately 2090 times higher than that of bare α -MnS and 50 times higher than that over β - In_2S_3 alone. The corresponding QE of this sample is as high as 34.2% at 450 nm even in the absence of any noble-metal co-catalysts. These results indicate the modification of compositions is a high efficient strategy to improve the photocatalytic activity. Furthermore, the addition of SO_3^{2-} and S^{2-} cannot only play a role as electron donors, but can also suppress the formation of yellow S_2^{2-} and solid S, favoring the long-term H_2 production. The activity of these newly reported sulfide photocatalysts could be further enhanced through the conventional routes such as loading of co-catalysts, doping other elements, which are expected to turn into practical

application for H_2 production using byproducts at petrochemical plants.

Acknowledgment

We thank financial supports by the National Natural Science Foundation of China (21403172), the Sino Swiss Science and Technology Cooperation (SSSTC, EG08-032015), the Sichuan Provincial International Cooperation Project (2017HH0030), Sichuan Youth Science and Technology Foundation (2014JQ0017) and the Innovative Research Team of Sichuan Province (2016TD0011).

Appendix A. Supplementary data

Supplementary data associated with this article can be found, in the online version, at [10.1016/j.apcatb.2017.06.019](https://doi.org/10.1016/j.apcatb.2017.06.019).

References

- [1] N.S. Lewis, D.G. Nocera, Proc. Natl. Acad. Sci. U. S. A. 103 (2006) 15729–15735.
- [2] J. Goldemberg, Science 315 (2007) 808–810.
- [3] A. Fujishima, K. Honda, Nature 238 (1972) 37–38.
- [4] A. Kudo, Y. Miseki, Chem. Soc. Rev. 38 (2009) 253–278.
- [5] X.B. Chen, S.H. Shen, L.J. Guo, S.S. Mao, Chem. Rev. 110 (2010) 6503–6570.
- [6] U.V. Kawade, R.P. Panmand, Y.A. Sethi, M.V. Kulkarni, S.K. Apte, S.D. Naik, B.B. Kale, RSC Adv. 4 (2014) 49295–49302.
- [7] S.A. Naman, S.M. Aliwi, K. Al-Emara, Int. J. Hydrogen Energy 11 (1986) 33–38.
- [8] Hydrogen Sulfide Human Health Aspects, Concise International Chemical Assessment Document 53, World Health Organization, Geneva, 2003.
- [9] A. Piéplu, O. Saur, J.C. Lavalley, O. Legendre, C. Nédez, Catal. Rev.: Sci. Eng. 40 (1998) 409–450.
- [10] I.A. Gargurevich, Ind. Eng. Chem. Res. 44 (2005) 7706–7729.
- [11] S.V. Tambwekar, M. Subrahmanyam, Int. J. Hydrogen Energy 22 (1997) 959–965.
- [12] J. Zaman, A. Chakma, Fuel Process. Technol. 41 (1995) 159–198.
- [13] J. Peng, Y. Zhou, H. Wang, H. Zhou, S. Cai, CrystEngComm 17 (2015) 1805–1812.
- [14] K. Yu, C. Zhang, Y. Chang, Y. Feng, Z. Yang, T. Yang, L. Lou, S. Liu, Appl. Catal. B 200 (2017) 514–520.
- [15] M.H. Hsu, C.J. Chang, Int. J. Hydrogen Energy 39 (2014) 16524–16533.
- [16] T. Hashimoto, H. Ohta, H. Nasu, A. Ishihara, Int. J. Hydrogen Energy 41 (2016) 7388–7392.
- [17] Y. Lan, Y. Lu, Z. Ren, Nano Energy 2 (2013) 1031–1045.
- [18] H.G. Yang, C.H. Sun, S.Z. Qiao, J. Zoum, G. Liu, S.C. Smith, H.M. Cheng, G.Q. Lu, Nature 453 (2008) 638–641.
- [19] N.S. Chaudhari, S.S. Warule, S.A. Dhanmane, M.V. Kulkarni, M. Valant, B.B. Kale, Nanoscale 5 (2013) 9383–9390.
- [20] F. Wang, S. Wei, Z. Zhang, G.R. Patzke, Y. Zhou, Phys. Chem. Chem. Phys. 18 (2016) 6706–6712.
- [21] A.P. Bhirud, S.D. Sathaye, R.P. Waichal, J.D. Ambekar, C.J. Park, B.B. Kale, Nanoscale 7 (2015) 5023–5034.
- [22] K.G. Kanade, B.B. Kale, J.O. Baeg, S.M. Lee, C.W. Lee, S.J. Moon, H. Chang, Mater. Chem. Phys. 102 (2007) 98–104.
- [23] E. Subramanian, J.O. Baeg, S.M. Lee, S.J. Moon, K.J. Kong, Int. J. Hydrogen Energy 34 (2009) 8485–9104.
- [24] M. Shelef, K. Otto, N.C. Otto, Adv. Catal. 27 (1978) 311–365.
- [25] J.P. Franck, G.P. Martino, Deactivation and Poisoning of Catalysis, in: J. Oudar, H. Wise (Eds.), Marcel Dekker Inc., New York, 1985, p. 205.
- [26] T. Kako, H. Irie, K. Hashimoto, J. Photochem. Photobiol. A: Chem. 171 (2005) 131–135.
- [27] M.C. Canela, R.M. Alberici, W.F. Jardim, J. Photochem. Photobiol. A 112 (1998) 73–80.
- [28] S. Kato, Y. Hirano, M. Iwata, T. Sano, K. Takeuchi, S. Matsuzawa, Appl. Catal. B 57 (2005) 109–115.
- [29] G. Ma, H. Yan, J. Shi, X. Zong, Z. Lei, C. Li, J. Catal. 260 (2008) 134–140.
- [30] X.F. Bai, Y. Cao, W. Wu, Renew. Energy 36 (2011) 2589–2592.
- [31] K.G. Kanade, J.O. Baeg, U.P. Mulik, D.P. Amalnerkar, B.B. Kale, Mater. Res. Bull. 41 (2006) 2219–2225.
- [32] U.V. Kawade, R.P. Panmand, Y.A. Sethi, M.V. Kulkarni, S.K. Apte, S.D. Naik, B.B. Kale, RSC Adv. 4 (2014) 49295–49302.
- [33] A. Bhirud, N. Chaudhari, L. Nikam, R. Sonawane, K. Patil, J.O. Baeg, B. Kale, Int. J. Hydrogen Energy 36 (2011) 11628–11639.
- [34] X. Liu, X. Liang, P. Wang, B. Huang, X. Qin, X. Zhang, Y. Dai, Appl. Catal. B 203 (2017) 282–288.
- [35] W. Shangguan, A. Yoshida, J. Phys. Chem. B 106 (2002) 12227–12230.
- [36] N. Bühl, K. Meier, J.-F. Reber, J. Phys. Chem. 88 (1984) 3261–3268.
- [37] C.D. Lokhande, A. Ennaoui, P.S. Patil, Thin Solid Films 330 (1998) 70–75.
- [38] C. Gümrüç, C. Ulutaş, R. Esen, Thin Solid Films 492 (2005) 1–5.
- [39] H. Wang, X. Yuan, Y. Wu, X. Chen, L. Leng, G. Zeng, RSC Adv. 5 (2015) 32531–32535.

[40] T. Zuo, Z. Sun, Y. Zhao, X. Jiang, X. Gao, *J. Am. Chem. Soc.* 132 (2010) 6618–6619.

[41] S. Cao, J. Zheng, J. Zhao, L. Wang, F. Gao, G. Wei, R. Zeng, L. Tian, W. Yang, *J. Mater. Chem. C* 1 (2013) 2540–2547.

[42] Q. Yuan, D. Liu, N. Zhang, W. Ye, H. Ju, L. Shi, R. Long, J. Zhu, Y. Xiong, *Chem. Int. Ed.* 56 (2017) 4206–4210.

[43] G. Xu, Y.L. Zhu, X.L. Ma, *Phys. Status Solidi A* 208 (2011) 123–128.

[44] S.J. Kim, H. Shibata, J. Takekawa, S.Y. Kitamura, K. Yamaguchi, Y.B. Kang, *Metall. Mater. Trans. B* 43 (2012) 1069–1077.

[45] H. Wang, X. Yuan, Y. Wu, G. Zeng, H. Dong, X. Chen, L. Leng, Z. Wu, L. Peng, *Appl. Catal. B* 186 (2016) 19–29.

[46] S. Rengaraj, S. Venkatraj, C.W. Tai, Y. Kim, E. Repo, M. Sillanpää, *Langmuir* 27 (2011) 5534–5541.

[47] K. Ikeue, S. Shiiba, M. Machida, *Chem. Mater.* 22 (2010) 743–745.

[48] K. Ikeue, S. Shiiba, M. Machida, *ChemSusChem* 4 (2011) 269–273.

[49] Y. Li, G. Chen, Q. Wang, X. Wang, A. Zhou, Z. Shen, *Adv. Funct. Mater.* 20 (2010) 3390–3398.

[50] J.S. Hu, L.L. Ren, Y.G. Guo, H.P. Liang, A.M. Cao, L.J. Wan, C.L. Bai, *Angew. Chem. Int. Ed.* 117 (2005) 1295–1299.

[51] J. Yu, J. Zhang, S. Liu, *J. Phys. Chem. C* 114 (2010) 13642–13649.

[52] J.G. Yu, J.F. Xiong, B. Cheng, S.W. Liu, *Appl. Catal. B* 60 (2005) 211–221.

[53] F. Dong, T. Xiong, Y.J. Sun, Y.X. Zhang, Y. Zhou, *Chem. Commun.* 51 (2015) 8249–8252.

[54] S. Yu, Y. Zhong, B. Yu, S. Cai, L. Wu, Y. Zhou, *Phys. Chem. Chem. Phys.* 18 (2016) 20338–20344.

[55] S. Todorova, H. Kolev, J.P. Holgado, G. Kadinov, C. Bonev, R. Pereniguez, A. Caballero, *Appl. Catal. B* 94 (2010) 46–54.

[56] Y. Li, G. Chen, Q. Wang, X. Wang, A. Zhou, Z. Shen, *Adv. Funct. Mater.* 20 (2010) 3390–3398.

[57] Z.Y. Zhao, Y. Zhou, F. Wang, K.H. Zhang, S. Yu, K. Cao, *ACS Appl. Mater. Interfaces* 7 (2015) 730–737.

[58] Y. Zhou, Z.Y. Zhao, F. Wang, K. Cao, D.E. Doronkin, F. Dong, J.-D. Grunwaldt, *J. Hazard. Mater.* 307 (2016) 163–172.

[59] L. Beyer, R. Kimse, J. Stach, R. Szargan, E. Hoyer, *Z. Anorg. Allg. Chem.* 476 (1981) 7–15.

[60] R.N. Sodhi, R.G. Cavell, *J. Electron. Spectrosc. Relat. Phenom.* 41 (1986) 1–24.

[61] B. Barbaray, J.P. Contour, G. Mouvier, *Environ. Sci. Technol.* 12 (1978) 1294–1297.

[62] G. Pandey, H. Sharma, S. Srivastava, R. Kotnala, *Mater. Res. Bull.* 46 (2011) 1804–1810.

[63] A. Kasahara, K. Nukumizu, G. Hitoki, T. Takata, J. Kondo, M. Hara, H. Kobayashi, K. Domen, *J. Phys. Chem. A* 106 (2002) 6750–6753.

[64] X. Zhang, Y. Du, Z. Zhou, L. Guo, *Int. J. Hydrogen Energy* 35 (2010) 3313–3321.

[65] M.Y. Liu, L.Q. Zhang, X.X. He, B. Zhang, H.F. Song, S.N. Li, W.S. You, *J. Mater. Chem. A* 2 (2014) 4619–4626.

[66] I. Tsuji, H. Kato, H. Kobayashi, A. Kudo, *J. Am. Chem. Soc.* 126 (2004) 13406–13413.

[67] F.-Y. Jou, F.D. Otto, A.E. Mather, *J. Chem. Eng. Data* 41 (1996) 1181–1183.

[68] C.D. Wagner, *Discuss. Faraday Soc.* 60 (1975) 291–300.

[69] S. Sun, J. Zhang, P. Gao, Y. Wang, X. Li, T. Wu, Y. Wang, Y. Chen, P. Yang, *Appl. Catal. B* 206 (2017) 168–174.

[70] H. Peisert, T. Chassé, P. Streubel, A. Meisel, R. Szargan, *J. Electron. Spectrosc. Relat. Phenom.* 68 (1994) 321–328.

[71] D.W. Hall, N.F. Borrelli, *J. Opt. Soc. Am. B* 5 (1988) 1654–1654.

[72] J.S. Jang, H.G. Kim, P.H. Borse, J.S. Lee, *Int. J. Hydrogen Energy* 32 (2007) 4786–4791.